

Journal of Geophysical Research: Solid Earth

RESEARCH ARTICLE

10.1002/2017JB014488

Special Section:

Seismic and micro-seismic
signature of fluids in rocks:
Bridging the scale gap

This article is a companion to Chen et al.
(2018), [https://doi.org/10.1002/
2017JB014491](https://doi.org/10.1002/2017JB014491).

Key Points:

- We propose an improved matching and locating technique to robustly detect and accurately locate weak microseismic events
- The novel approach further enhances the detectability of microseismic events as compared with the matched filter analysis
- The proposed approach significantly improves the location precision of weak microseismic events, particularly the depth accuracy

Correspondence to:
H. Chen,
chchao@cup.edu.cn

Citation:
Meng, X., Chen, H., Niu, F., Tang, Y., Yin, C., & Wu, F. (2018). Microseismic monitoring of stimulating shale gas reservoir in SW China: 1. An improved matching and locating technique for downhole monitoring. *Journal of Geophysical Research: Solid Earth*, 123. <https://doi.org/10.1002/2017JB014488>

Received 30 MAY 2017
Accepted 13 OCT 2017
Accepted article online 12 FEB 2018

Microseismic Monitoring of Stimulating Shale Gas Reservoir in SW China: 1. An Improved Matching and Locating Technique for Downhole Monitoring

Xiaobo Meng¹, Haichao Chen¹ , Fenglin Niu^{1,2} , Youcai Tang¹ , Chen Yin³, and Furong Wu³

¹Unconventional Natural Gas Institute and State Key Laboratory of Petroleum Resources and Prospecting, China University of Petroleum, Beijing, China, ²Department of Earth, Environmental and Planetary Sciences Rice University, Houston, TX, USA, ³CNPC Sichuan Geophysical Company, Chengdu, China

Abstract We introduce an improved matching and locating technique to detect and locate microseismic events ($-4 < M_L < 0$) associated with hydraulic fracturing treatment. We employ a set of representative master events to act as template waveforms and detect slave events that strongly resemble master events through stacking cross correlograms of both P and S waves between the template waveforms and the continuous records of the monitoring array. Moreover, the residual moveout in the cross correlograms across the array is used to locate slave events relative to the corresponding master event. In addition, P wave polarization constraint is applied to resolve the lateral extent of slave events in the case of unfavorable array configuration. We first demonstrate the detectability and location accuracy of the proposed approach with a pseudo-synthetic data set. Compared to the matched filter analysis, the proposed approach can significantly enhance detectability at low false alarm rate and yield robust location estimates of very low SNR events, particularly along the vertical direction. Then, we apply the method to a real microseismic data set acquired in the Weiyuan shale reservoir of China in November of 2014. The expanded microseismic catalog provides more easily interpretable spatiotemporal evolution of microseismicity, which is investigated in detail in a companion paper.

1. Introduction

Over the last decade, microseismic monitoring ($-4 < M_L < 0$) has been the primary technology to diagnose the efficiency of hydraulic fracturing treatment within stimulated unconventional reservoirs (Duncan & Eisner, 2010; Maxwell et al., 2010; Warpinski, 2009). The abundant low-magnitude microseismic events, due to the power law scaling of earthquake occurrence with magnitude, are of prominent importance for quantifying the spatial extent (e.g., fracture orientation, length, and heights) and complexity (e.g., fracture density and connectivity) of hydraulic fractures within the stimulated rock volume of the target formation (Williams-Stroud et al., 2013).

However, most microseismic events are typically characterized by low signal-to-noise ratio (SNR). It is thereby notoriously difficult to reliably detect and accurately locate these tiny but abundant events, even in the case of deep downhole monitoring, which generally provides higher quality data than surface monitoring owing to the close proximity of the sensors to the treatment zone (Maxwell et al., 2010). Microseismic events can easily be masked in the presence of strong ambient noise from various sources, most notably from the bore-hole waves excited by pumps located at the surface and instrument self-noise (Vaezi & van der Bann, 2014). As a consequence, a large portion of events are single phase events, that is, events where only a single phase (typically the S wave) is readily discernible, or even completely invisible. Hence, conventional processing requires a significant level of artificial interaction and suffers from high false triggers if using an aggressive threshold (Akram & Eaton, 2016). Thus, in practice, only a small number of microseismic events that show clear P and S wave arrivals are commonly used for source location and subsequent interpretation.

Recently, the pervasive use of microseismic monitoring has stimulated the development of two categories of coherence-based detectors, which exploit the waveform coherency of a single event over different stations (migration based) and multiple events at one station (template based), respectively. The two coherence-based detectors circumvent the cumbersome phase picking and thus significantly lower the detection threshold of microseismic events. The migration-based technique, also known as the source-scanning algorithm (SSA), detects events based on the stacked energy of a characteristic function (e.g., envelope

and Short-time average over long-time average (STA/LTA) function of continuous waveforms) over gridded potential source locations and origin times (Gharti et al., 2010; Grigoli et al., 2013, 2016; Kao & Shan, 2004; Liao et al., 2012). It provides robust location estimates of microseismic events even in the presence of strong ambient noise and thereby has been extensively used in surface microseismic monitoring (Drew et al., 2013; Pesicek et al., 2014; Trojanowski & Eisner, 2016). Nevertheless, it is still subject to high false alarm rates, and the location accuracy strongly depends on the local velocity structure. Besides, the detectability of the migration-based technique is significantly compromised without accounting for the radiation pattern of shear sources, especially when a monitoring array cover a wide range of azimuths. Simple stacking of original signals with strong amplitude and polarity variations resulted from complex radiation pattern may lead to missing weak microseismic events. Hence, various optimal stacking techniques, such as envelope stacking (e.g., Caffagni et al., 2016), STA/LTA characteristic function stacking (e.g., Drew et al., 2013), and source mechanism correction (e.g., Anikiev et al., 2014; Stanek et al., 2015), have been proposed to overcome source mechanism effects and thus ensure constructive stacking across large-aperture arrays.

The template-based technique, also referred to as matched filter analysis (MFA), employs a set of well-located high-SNR representative events to act as master events and detects slave events through stacking cross correlograms between the template waveforms and continuous records of multiple receivers and components (Gibbons & Ringdal, 2006). It is shown to be an exquisitely sensitive and discriminative technique for detecting and characterizing low-magnitude events that strongly resemble to proximal master events, having high detection probability at low false triggers even in the presence of strong correlated and uncorrelated noise. As a consequence, the MFA has been broadly employed to investigate intensive aftershocks (e.g., Peng & Zhao, 2009) and nonvolcanic tremors (e.g., Shelly, 2010; Shelly et al., 2007). Previous studies have shown that microseismic events induced by hydraulic fracturing are commonly spatially and temporally clustered, possibly related to repeated shear slip on a fracture or neighboring subparallel fractures (Rutledge & Phillips, 2003). Therefore, the MFA has also been widely utilized to obtain detailed spatiotemporal distribution of induced seismicity related to fluid injections (Bao & Eaton, 2016; Caffagni et al., 2016; Eaton & Caffagni, 2015; Skoumal et al., 2015; Song et al., 2010; van der Elst et al., 2013).

It is known that selecting proper master events play an essential role in enhancing the detectability of the MFA. However, the selection of optimal master events is not a trivial task. It is computationally expensive or even prohibitive to use all the events obtained by conventional energy detectors (e.g., the classic STA/LTA algorithm) as master events. Usually, master events are a subset of the events, and only the events with SNR exceeding a predefined threshold are considered as potential candidates. Although the choice of master events is to some extent arbitrary, it is generally recognized that the master events should have distinctive waveforms characteristics to avoid duplicate detection, that is, a slave event is detected by multiple master events. Thus, master events with proximal locations and virtually identical source mechanisms are avoided. For instance, in the case of downhole microseismic monitoring of hydraulic fracturing stimulation, Caffagni et al. (2016) suggested that four uniformly distributed master events for each treatment stage are sufficient for their study. An alternative technique for obtaining representative template waveforms is the so-called subspace method, which is a generalization of the template-based detection that exploits feature common to a set of clustered events (Barrett & Beroza, 2014; Song et al., 2014). Although the template waveforms from the subspace method shows superior performance over individual master event by permitting greater waveform variability, we cannot relatively locate the detected slave events with respect to the master events. Moreover, the typical MFA assumes that the target events are collocated with the corresponding master event, and the stacking of correlograms is performed without moveout correction. Recently, Zhang and Wen (2015) proposed a modified MFA, termed as Matched & Locate (M&L) method, which employed the residual moveout in the correlograms across the array to locate identified events relative to the master event. The M&L method not only improves the location accuracy of weak events but also further enhance the detectability by virtue of allowing larger interevent separation. Nevertheless, the regular M&L method is not capable of resolving the relative location of a matched event in the case of unfavorable array geometry, such as linear downhole array.

In this study, we develop an improved matching and locating technique (iMLT) to detect and locate weak microseismic events, specifically tailored to downhole array configuration. We employ the cross correlograms of both *P* and *S* waves between the template waveforms of the master event and the continuous records of each component at each receiver, which are subsequently stacked along differential moveouts to obtain

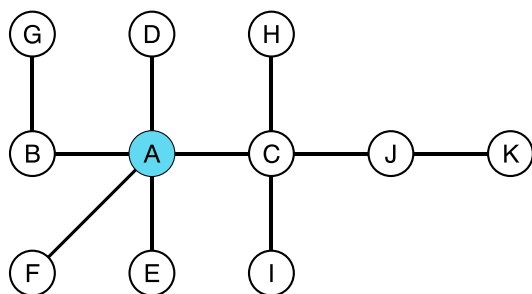


Figure 1. Schematic diagram of an identified cluster. The microseismic events are denoted as lettered circles, and the solid lines that connect events indicate identified doublets. The event that is doublet with the maximum number of events (blue circle) is chosen as the potential candidate of master event.

coherence functions. *P* wave polarization constraint is utilized to improve lateral resolution in the case of linear downhole array geometry. We detect and locate the weak microseismic events relative to their corresponding master event by maximizing the coherence value within a 3-D searching volume around the master's hypocenter.

The paper is organized as follows: we first describe the procedures of the proposed approach in section 2 and then benchmark the approach with observed microseismic events and a set of pseudo-synthetic events in section 3. In section 4, we apply the method to a subset of the continuous records from a field microseismic monitoring experiment. Finally, we discuss the advantages of the proposed approach over the other coherence-based methods in section 5. The detailed spatiotemporal evolution of the microseismicity during the whole treatment stage, as well as its possible relation to the fluid injection activity, is presented in a companion paper (Chen et al., 2018).

2. Data and Methodology

2.1. Selection of Master Events

Similar to the MFA, our approach employs a set of well-located master events with representative template waveforms to detect and locate small events embedded in continuous records. The selection of a suitable set of master events is of great importance. In principle, the master events should form a complete basis for all of the detectable microseismicity, representing all observed source mechanisms and wide range of hypocentral locations. The following procedures illustrate briefly how the master events are selected.

Generally following Arrowsmith and Eisner (2006), all the events obtained with a standard STA/LTA algorithm are clustered employing a chainlike clustering algorithm. Events are first manually picked and relocated, resulting in consistent data set in terms of picking errors. We also estimate the local magnitude M_L of the events with equation (1) (Hutton & Boore, 1987).

$$M_L = \log_{10}(A) + 1.11 \log_{10}(R) + 0.00189 \times R - 2.09 \quad (1)$$

where A and R indicate the peak amplitude of *S* wave and viewing distance from the geophone, respectively. Then, we calculate the normalized correlation coefficient for all possible event pairs by sliding a template waveform of the first event over a selected time window of the second event and recording the maximum averaged correlation coefficient of three components. For the sake of simplicity, we used a uniform time window length (0.5 s) for all receiver levels in this study, which starts at 0.1 s before *P* wave arrival and is long enough to contain both *P* and *S* waves. The definition of doublet is somewhat subjective, since the requirement of similarity depends on the specific application. In this study, we empirically use a correlation threshold of 0.55 to identify the doublets. A multiple is defined as a cluster of events where each event is a doublet with at least one other event in the multiple. This definition of multiple does not require mutual similarity among all events within a multiple but allows for chainlike similarity. We argue that this relatively loose rule is preferable to the stricter one that requires all events in a multiple be mutually similar, which tends to yield a large number of small clusters or stand-alone events.

For a given cluster, we choose the most prolific event as the potential candidate of master event. Figure 1 illustrates the schematic diagram of an identified cluster. The most prolific event within one cluster is defined as the one that is doublet with the maximum number of events, which is likely to provide more representative template waveforms. This enables us to substantially reduce the number of master events that are highly mutually correlated and do not provide additional information. Furthermore, the master event should also meet an additional criterion: a minimum SNR of 2 (*P* wave) over all components.

Occasionally, the events of one cluster may spread out over a large region, possibly due to the chainlike cluster algorithm. In this scenario, more than one master event within the cluster is needed based on their spatial proximity, in order to obtain spatially uniform distribution of master events. We exclude the selected master events, as well as the events in the neighborhood of the master events and then repeat the above procedure to choose the most prolific event from the remaining events within the cluster. In this study, the minimum

hypocentral separation between two master events is empirically set to be 50 m, which is approximately equivalent to one wavelength of the dominant frequency (~ 100 Hz).

2.2. Detection and Location

2.2.1. Coherence Functions

We first calculate normalized cross correlograms of both P and S waves of the template waveforms of each component at each station against their respective continuous records in frequency domain, which can be expressed as

$$C_{ij}(\tau) = \frac{F_D^{-1}\left(m_{ij}^*(f)s_{ij}(f)\right)}{\sqrt{\sum_t m_{ij}^2(t) \sum_t s_{ij}^2(t)}} \quad (2)$$

where F_D^{-1} represents the inverse Fourier transform and $m_{ij}(t)$ and $s_{ij}(t)$ represent the template waveform of P or S wave and continuous record of the j th component at the i th receiver level, respectively. It is noted that cross correlograms are calculated in frequency domain to enhance computational efficiency. Moreover, the cross correlograms of P and S waves are calculated separately, instead of a time window that encompasses both the P and S waves. An important parameter is the size of the time window. The smaller the window length, the more likely that some arbitrary wave trains of the continuous records can match the template waveforms. In contrast, a long window may lead to cycle skipping. Based on our experience, 2 to 4 times the dominant period is recommended. We thereby use a 0.03 s long time window for both P and S wave. Note that the averaged cross correlograms of P wave comes from all three components, while that of S wave is evaluated by averaging the cross correlograms of the two orthogonal horizontal components (equation (3)). This produce cross correlograms of P and S waves for each record level over the time processed.

$$\begin{aligned} \bar{C}_i^P(t) &= \frac{1}{3} (C_i^{P,Z} + C_i^{P,N} + C_i^{P,E}) \\ \bar{C}_i^S(t) &= \frac{1}{2} (C_i^{S,N} + C_i^{S,E}) \end{aligned} \quad (3)$$

Next, we stack all the averaged cross correlograms of both P and S waves over the monitoring array along differential moveouts to obtain the coherence functions. Assuming that a master event \mathbf{M} has been accurately located at \mathbf{r}_m , we set up a meshed 3-D region centered at the location of the master event and each grid node is considered to be a potential source position of a slave event. As a rule of thumb, the waveform similarity between two events, whose source mechanisms are virtually identical, is not greatly affected by velocity heterogeneities along the raypaths, as long as the event separation is less than one-fourth wavelength of the dominant frequency (Waldhauser & Ellsworth, 2000). It is speculated that this basic assumption should still be valid when the interevent distance reaches a few wavelengths of the dominant frequency, which is much smaller than the distance between the sources and a common receiver (Grigoli et al., 2016; Zhang & Wen, 2015). Thus, we can extend the slave events to larger hypocentral separation, instead of a rather restricted volume (the first Fresnel zone) in the neighborhood of the master event. Assuming that the averaged P wave velocity is 4,000 m/s and the dominant frequency is 100 Hz, the wavelength is ~ 40 m. In this study, we set the grid boundary to be 100 m. For each virtual source k close to the master event, the corrected traveltime of both P and S waves, which includes the picked arrival of the master phase and the theoretical travelttime difference predicted based on the relative location between the virtual source and the master event, are calculated and stored in a 3-D relative travelttime table.

$$\tau_{ik} = t_i^o(\mathbf{r}_m) + t_i^c(\mathbf{r}_k) - t_i^c(\mathbf{r}_m) \quad (4)$$

where $t_i^o(\mathbf{r}_m)$ is the picked arrival of the master event and $t_i^c(\mathbf{r}_m)$ and $t_i^c(\mathbf{r}_k)$ are the theoretical travelttime from the i th receiver to the hypocenter of the master event and the k th virtual source, respectively. Then, we align the cross correlograms along the corrected moveout, and stack them for both P and S waves over all receiver levels to enhance the SNR of the coherence function $C(\mathbf{r}_k, t)$ of each virtual source (equation (5)).

$$C(\mathbf{r}_k, t) = \frac{1}{2N} \sum_{i=1}^N (\bar{C}_i^P(t + \tau_{ik}^P) + \bar{C}_i^S(t + \tau_{ik}^S)) \quad (5)$$

where N is the number of the receiver levels. The coherence function is a measure of the coherence between the continuous records and the template waveform of master events for different locations and origin times. We thus obtain a map of coherence in space and time.

In the case of a single monitoring well, which is pervasive in downhole monitoring, we add the P wave polarization constraint to resolve the horizontal extent of potential events. We define an azimuthal probability density function $\Phi_{ik}(t)$ as

$$\Phi_{ik}(t) = \exp\left\{-\sigma((\phi_{ik}^c - \phi_{im}^c) - (\phi_{ik}^o - \phi_{im}^o))^2\right\} \quad (6)$$

where σ is a scaled parameter and is empirically set to be 50 and ϕ_{im}^c and ϕ_{ik}^c are the theoretical back azimuth of the master event and the virtual source at the i th receiver level, respectively, which are determined based on the source-receiver geometry. ϕ_{im}^o and ϕ_{ik}^o are the P wave polarization angle of the template waveforms and continuous records, respectively. To calculate the observed P wave polarization angle, we build the covariance matrix of the three-component records for a time window enclosing the P wave signal and then solve the eigenvalues and eigenvectors of the covariance matrix. The eigenvectors associated with the largest eigenvalue correspond to the direction of the largest linear polarization. Then, a composite coherence function can be modified from equation (5) and defined as

$$C(\mathbf{r}_k, t) = \frac{1}{N} \sum_{i=1}^N \left\{ \omega \Phi_{ik}(t + \tau_{ik}^P) + (1 - \omega) \frac{\bar{C}_i^P(t + \tau_{ik}^P) + \bar{C}_i^S(t + \tau_{ik}^S)}{2} \right\} \quad (7)$$

where ω is the weight factor of the azimuthal probability density function and is empirically set to be 0.1 in our study.

2.2.2. Detection and Location of Slave Events

Similar to the MFA, we also use a multiple of the median absolute deviation (MAD), a robust outlier detector, to set the user-specified detection threshold (Peng & Zhao, 2009). For each virtual source, we compute the MAD of the coherence function over each 10 min time window and set the threshold value at nine times of the MAD. It is noted that the MAD is generally independent of time window length. A trigger is declared if the coherence value exceeds the threshold value. Assuming that the minimum time interval between two events is 0.5 s, triggers separated by less than 0.5 s are consolidated to avoid false alarms. Furthermore, the location of the detected slave events relative to the master event is determined by maximizing the coherence value of the coherence image within the 3-D searching volume around the master's hypocenter. Hypocenters located on the searching boundary are discarded. There is trade-off between the number of valid detections and the possibility of false triggers. The probability of exceedance for nine times the MAD is 6.4×10^{-10} for a normally distributed random variable (Peng & Zhao, 2009). In our study, we have 172,800,000 samples (2,000 sps) in a 1 day period. So the chance of spurious detection for each master event is less than one event per day, which implies that most of the detections are valid microseismic events. Occasionally, one slave event might be detected by multiple master events. We remove the duplicate slave events by retaining the master-slave pair associated with the highest coherence value.

Once a slave event is detected and located, its relative magnitude is estimated based on the peak amplitude ratio of the stacked envelope along the corrected moveout over the monitoring array, with respect to the corresponding master event. Assuming that a tenfold increase in amplitude corresponds to one-unit increase in magnitude, the relative magnitude of the slave event can be estimated using equation (8) after correcting for geometrical spreading (Caffagni et al., 2016).

$$dM = \log_{10}\left(\frac{A_s}{A_m} \cdot \frac{d_s}{d_m}\right) \quad (8)$$

where A_s and A_m denote the peak S wave amplitude of the stacked envelope of the slave event and the master event, respectively, and d_s and d_m indicate the distance from the nearest receiver level to the hypocenter of the slave event and master event, respectively.

3. Benchmark Analysis

In this section, we first benchmark our approach with two closely located microseismic events from a field monitoring experiment, illustrating its effectiveness and superior performance over the matched filter analysis. Then, we demonstrate the detectability and location resolution of the method with pseudo-synthetic events generated by adding observed seismic noise to scaled waveforms of a high-SNR microseismic event.

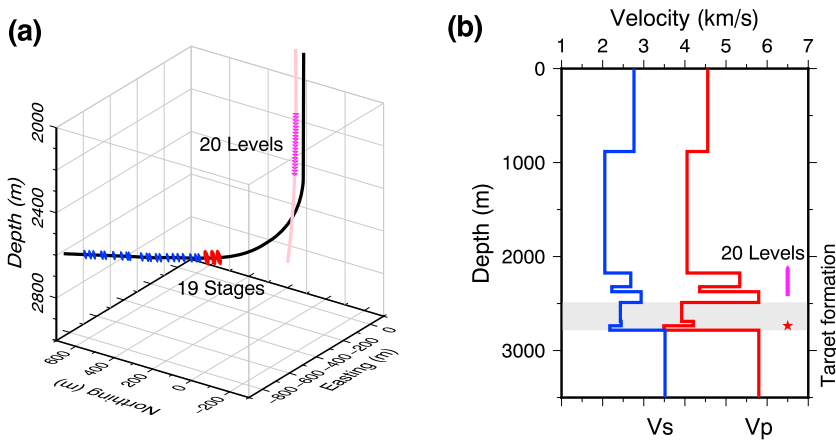


Figure 2. (a) The 3-D view of the field experiment geometry. The wellhead of the monitoring well (pink line) is laterally separated from that of the treatment well (black line) by about 50 m. The downhole monitoring array (purple triangles) consists of 20 levels of triaxial 15 Hz geophones at a depth from 2,120 m to 2,405 m with sensor spacing of 15 m, about 300 m above the perforation shots of the studied treatment stage (solid red ellipsoids). The distance between the perforation shots and the lowest geophone is ~500 m. (b) Layered P wave (thick red line) and S wave (thick blue line) velocity profile used for event location. The target shale formation is denoted as gray shadow and the depth of the monitoring array (purple triangles) and perforation shots (red star) are also shown for reference.

3.1. Field Experiment

A microseismic survey was performed during the 19-stage hydraulic fracturing stimulation of a pilot horizontal well within the shale play in southwest Sichuan basin of China between 28 October and 10 November of 2014. Microseismic monitoring was accomplished by a temporary string of sensors in a vertical monitoring well, whose wellhead is in close proximity (~50 m) to that of the treatment well (Figure 2a). The receiver array consists of 20 levels of triaxial 15 Hz geophones deployed at a depth from 2,515 m to 2,800 m, with sensor spacing of 15 m and a sampling rate of 2,000 Hz. In this study, we used a subset of the continuous downhole data set during the last fracturing stage (the nineteenth stage), which is located near the heel region and is closely proximal to the downhole monitoring array. Three consecutive perforation shots were fired before the hydraulic pumping of slick water (red ellipsoids in Figure 2). The distance between perforation shots and the geophones is in the range between 500 m and 720 m. We first used the signal of the first perforation shot to check the orientation of each sensor. Then, we rotated the recorded data to Z-N-E coordinate for further analyses. We employed a 1-D velocity model that was derived from the compressional and shear sonic logs of the vertical monitoring well and further calibrated by the arrival times of the first perforation shot of the treatment stage (Figure 2b).

We first band-pass filtered the continuous downhole records during the last injection stage between 20 Hz and 500 Hz to eliminate low- and high-frequency noise not related to microseismic signals. Then, the continuous data set was initially processed using a standard STA/LTA algorithm, which resulted in a total of 397 detected events. There are numerous events where both P and S wave arrivals are visible but hard to be picked accurately due to low SNR and complicated waveforms. Of a total of 397 events, 240 events with good SNR could be confidently located, with magnitude range from -3.0 to 1.3 (Figure 3). The hypocentral distribution of the located events exhibits strong spatial clustering, with more events to the northeast side of the injection interval. It is noted that the viewing distance between the events and the deepest receiver level ranges from 480 m to 680 m.

3.2. Microseismic Events

We selected two closely located microseismic events that are well recorded by the downhole array. Figure 4 shows the three-component waveforms of the master event (red) that occurred at 08:03:07 on 10 November 2014 ($M_L 0.73$), as well as the target event (black) that occurred at 09:06:05 on 10 November 2014 ($M_L -0.25$). Despite its smaller magnitude, it is obvious that the waveforms of the target event are remarkably similar to that of the master event.

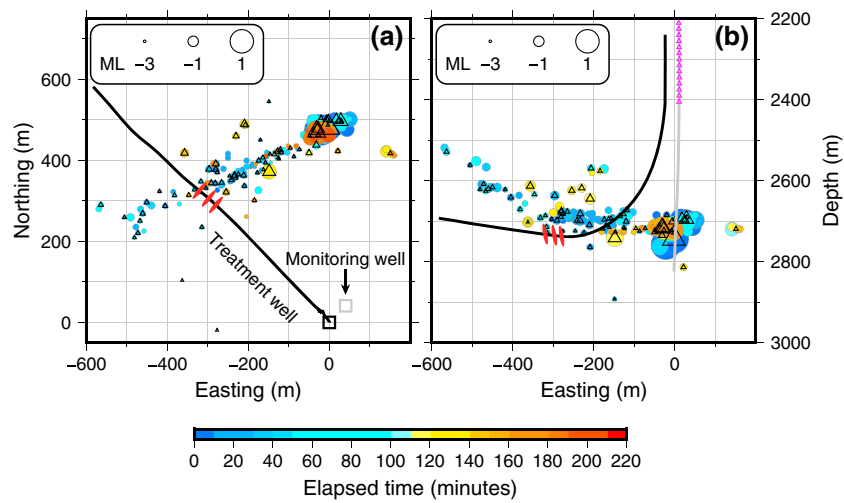


Figure 3. (a) Map view and (b) depth view of the hypocentral distribution of microseismic events during the nineteenth stage of hydraulic fracturing treatment. The well trajectory of the treatment well (black line) and the monitoring well (gray line), as well as the locations of the perforation shots (red ellipsoids), is shown for reference. Events are color coded by occurrence with respect to the onset of injection and scaled by local magnitude. The open triangles represent the master events.

We first use only P wave of the master event to obtain the coherence image (Figure 5a), neglecting the cross correlograms of S wave in equation (7). While the map view (left panel of Figure 5a) and the north view (right panel of Figure 5a) of the coherence image present two concentrated spots, the east view (center panel of Figure 5a) of the coherence image reveals an obliquely extending streak, indicating that the focal depth is less well constrained. We speculate that the spread of the coherence values results from the trade-off between the origin time and focus depth and could be mitigated with increased azimuthal coverage of

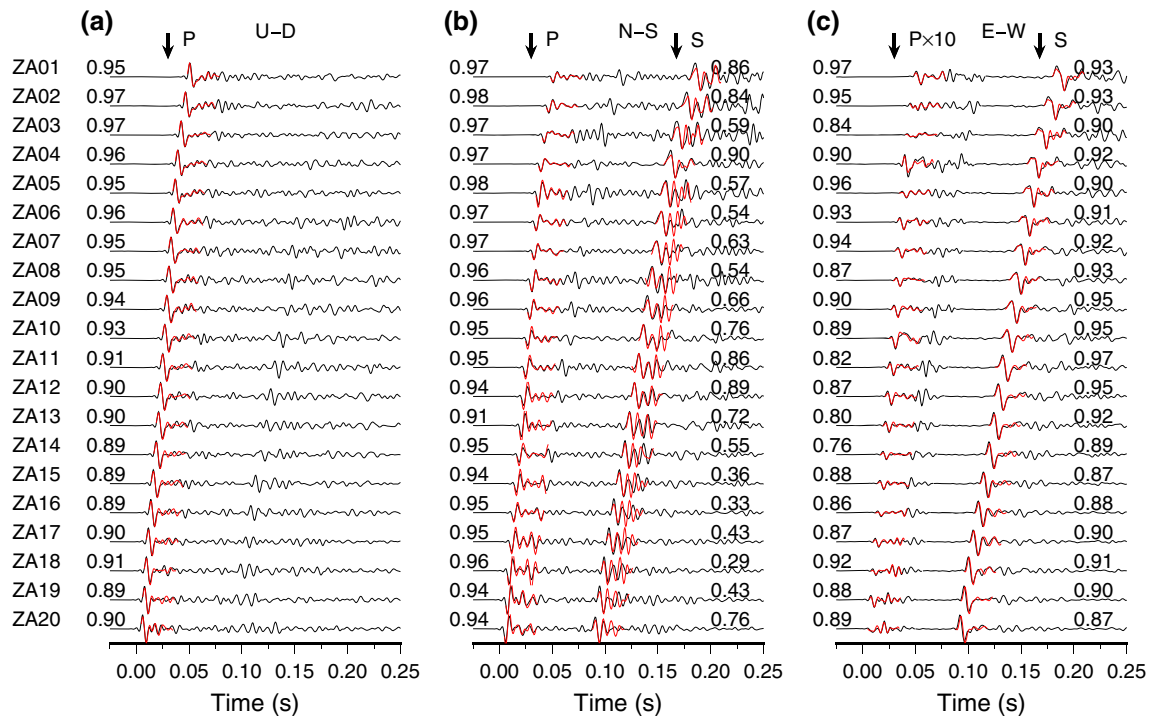


Figure 4. Waveform comparison between the master event (red) and the target slave event (black) for the three components of the 20 receiver levels. (a) U - D component, (b) N - S component, and (c) E - W component. The name of the receiver level, as well as the cross-correlation coefficients of P and S wave, is labeled besides the corresponding waveform. Note that the P wave waveforms of the E - W component are upscale by 10 times for the purpose of presentation.

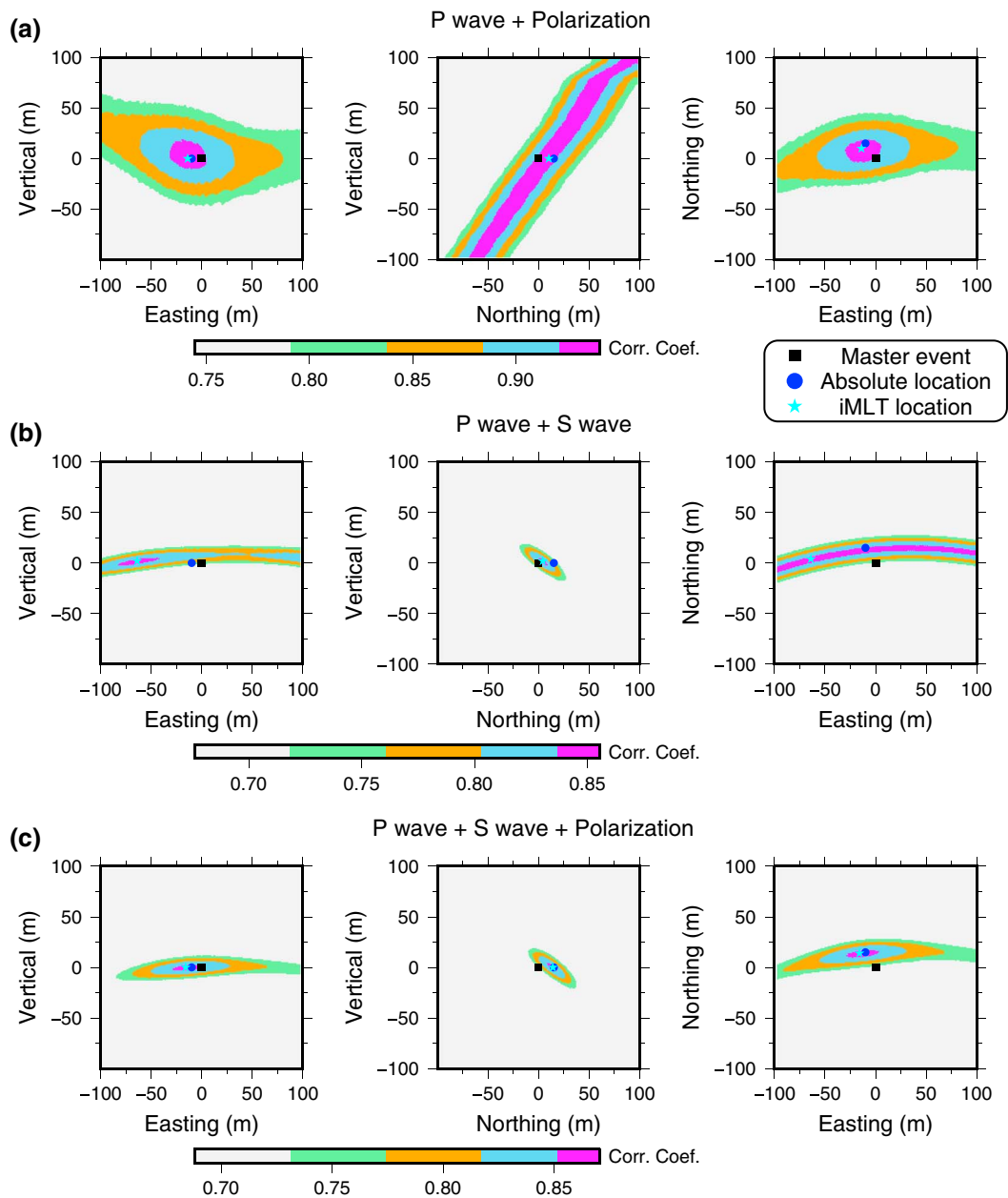


Figure 5. The contour maps of the mean coherence value in three plane view in the case of (a) using P wave cross correlograms with polarization constraint, (b) using both P and S wave cross correlograms without polarization constraint, and (c) using both P and S wave cross correlograms with polarization constraint. It is noted that we only plot the region within 80% of the maximal coherence value for sake of clarity. The location of the master event is indicated by solid black square. The absolute location determined with manually picked arrivals and the matched location from our approach of the target event are denoted as blue circle and cyan asterisk, respectively.

monitoring array, for example, two azimuthally separated linear downhole array. In spite of the spread of the coherence values, the matched location of the target event is still quite close to the absolute location determined with manually picked arrivals, suggesting that our approach can locate single-phase event with reasonable accuracy. Then, we showed the coherence image using both P and S wave without the P wave polarization constraint (Figure 5b). While the focus depth is well confined (left and middle panels of Figure 5b), the coherence image spreads out in the easting direction, illustrating the importance of implementing P wave polarization constraint, especially in the case of linear downhole array. Finally, we obtained the coherence image using both P and S waves, as well as the P wave polarization constraint (Figure 5c). It is

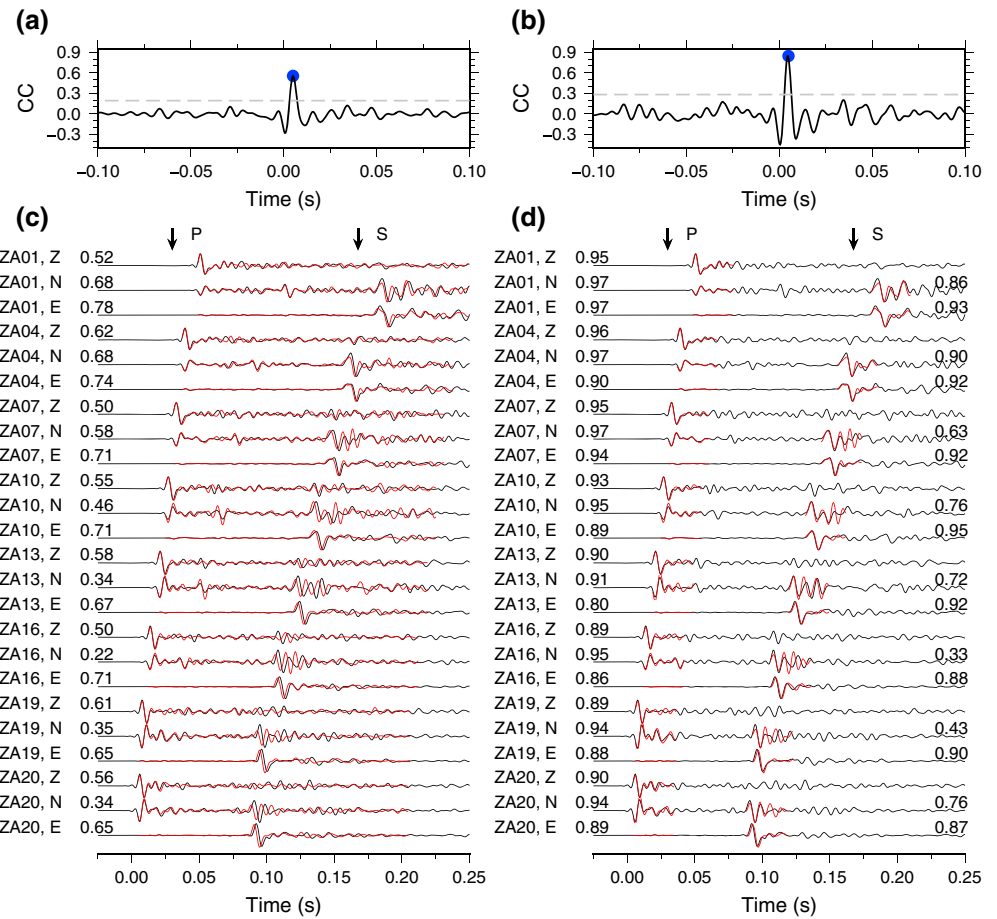


Figure 6. (a and b) Stacked cross correlograms and (b and d) waveform comparison between the master event (red) and the target slave event (black) for the three components of several selected receiver levels. The results of the matched filter analysis (a and c) and our approach (b and d) are shown for comparison.

shown that the coherence images are remarkably sharper, exhibiting a well-defined maximum, as opposed to a wide streak when only P wave was used. The matched location of the target event almost coincides with its absolute location, implying high resolution on the location of the target event. The hypocentral distance can be well constrained by S - P traveltimes, and thus, the focus depth is significantly better confined.

Figures 6a and 6b presents the comparison of the stacked cross correlograms between the MFA and the iMLT. Figure 6c shows the waveform comparison of the MFA between the master event and the target event for several selected receiver levels. Since the target event is approximately 18.0 m away from the master event, the waveforms from the two events cannot be aligned coherently, ascribed to the different S - P traveltimes of the two events across the monitoring array, leading to lower and wider stacked cross correlogram (Figure 6a). In contrast, we can obtain a higher and more impulsive stacked cross correlogram, due to the more coherence energy in the individual cross correlogram over the monitoring array (Figure 6d). This example also highlights the significance of calculating the cross correlograms of P and S waves separately.

3.3. Pseudo-Synthetic Events

We further test the method's capability to detect and locate low-SNR events using a set of pseudo-synthetic events. Since the commonly used white noise cannot account for the spatial and temporal variations of seismic noise under field condition (Birnie et al., 2016), we generate the pseudo-synthetic events by scaling down the high-SNR target event used in the previous subsection and immersing it into real seismic noise. Assuming that a tenfold increase in amplitude corresponds to one-unit increase in magnitude, we can synthesize the slave events with a wide range of local magnitudes.

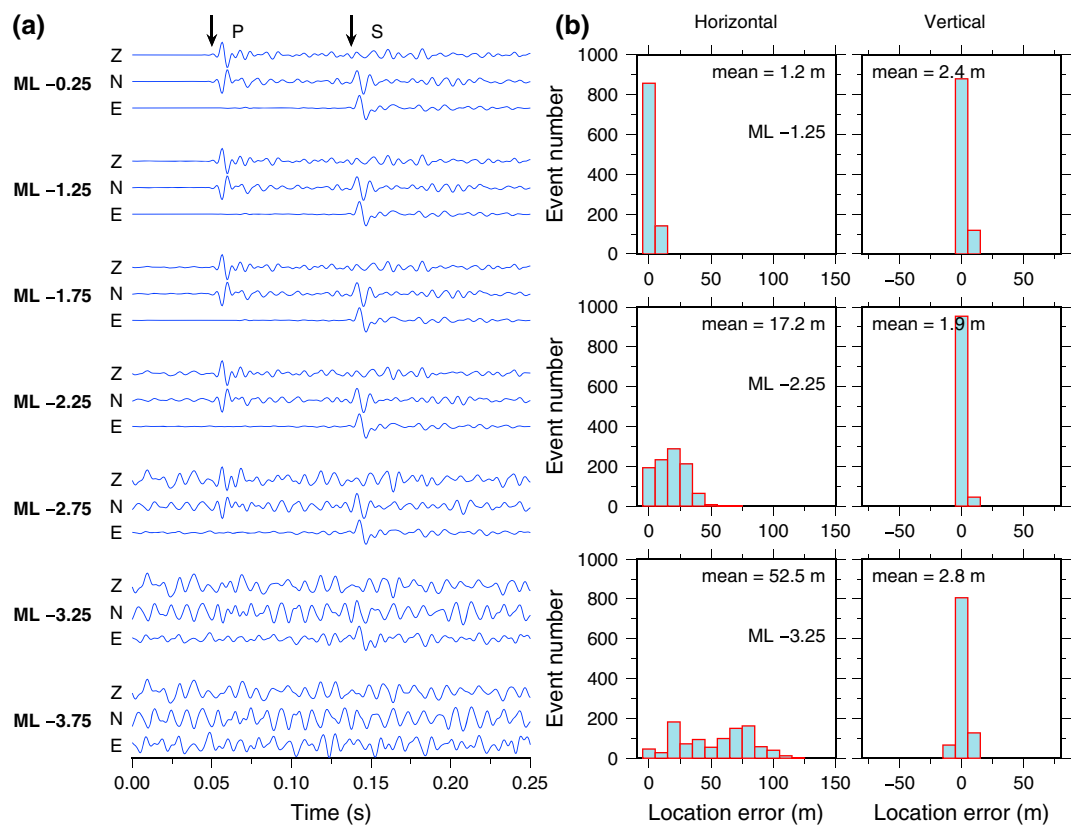


Figure 7. (a) Example waveforms of pseudo-synthetic events at various magnitude levels recorded at the deepest receiver level, which are obtained by scaling down waveforms of the target event in Figure 4 and superimposing the observed ambient seismic noise. The magnitudes of the pseudo-synthetic events are marked on the left side of the corresponding waveforms. (b) Histogram distribution of the horizontal (left column) and vertical (right column) positional errors of 1,000 pseudo-synthetic events at the magnitude level of -1.25 , -2.25 , and -3.25 , respectively. The mean positional error of all the detected events is also marked in the top of each panel.

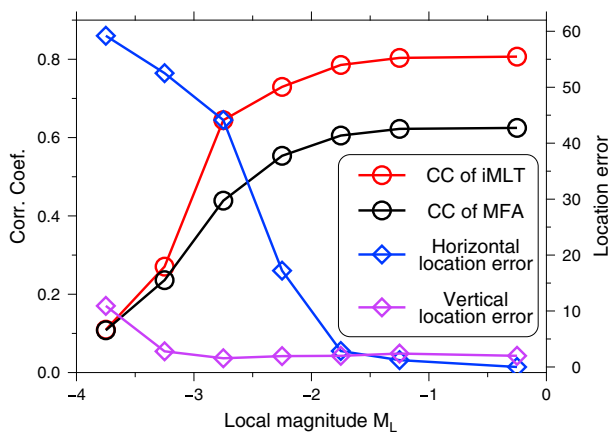


Figure 8. The mean coherence values of all detected pseudo-synthetic events as a function of local magnitude from the matched filter analysis (MFA) (black circles) and the improved matching and locating technique (iMLT) (red circles). The blue and purple diamonds indicate the mean horizontal and vertical positional error of pseudo-synthetic events, respectively. CC = correlation coefficient.

Figure 7a shows one of the 1,000 pseudo-synthetic events at various magnitude levels. Similar to the previous example, we use the master event to detect and locate the pseudo-synthetic events. In the scenario of $M_L = -3.25$, both the P and S waves are hardly visible. Thus, these events cannot be detected with conventional energy detectors. However, both the MFA and our approach can still robustly detect all the pseudo-synthetic events without false alarms. Moreover, in the scenario of $M_L = -3.75$, 969 out of 1,000 pseudo-synthetic events are detected by the iMLT and only 727 events are detected by the MFA, indicating that our approach is still effective for the extremely low SNR events that cannot be detected with the MFA. Figure 8 presents the mean coherence value of all detected pseudo-synthetic events as a function of the local magnitude from the MFA (black circles) and our approach (red circles), respectively. It is shown that our approach has notably higher coherence values than the MFA.

Figure 7b shows the histogram distribution of the horizontal and vertical positional errors at the magnitude level of -1.25 , -2.25 , and -3.25 , respectively. The mean positional error of all the detected events is also marked in the top of each panel. In the scenario of $M_L = -1.25$, all events are accurately located, implying that the location estimates are unbiased. As evident from Figure 8, the horizontal positional error

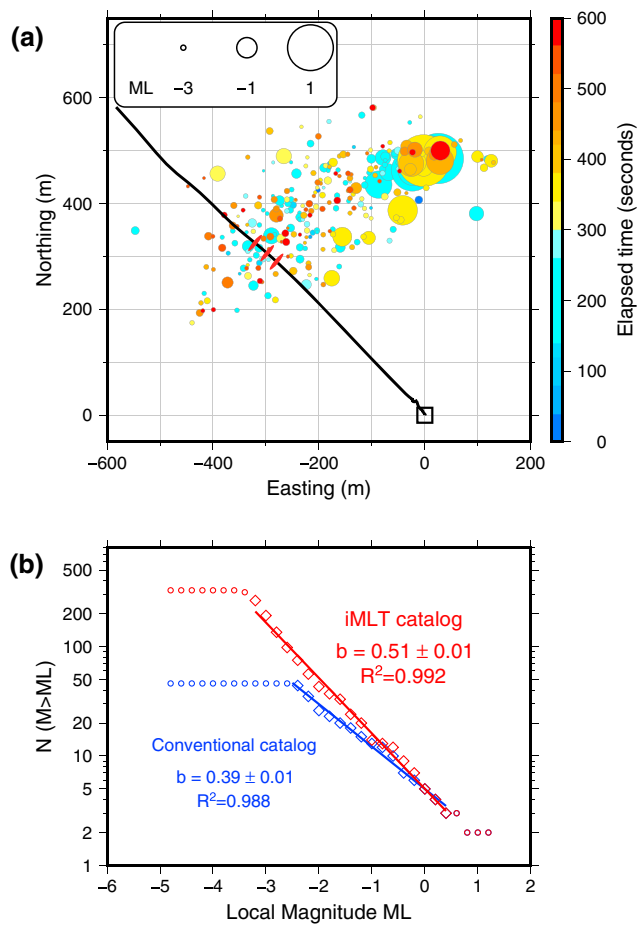


Figure 9. (a) Map view of the hypocentral distribution of the detected events within the first 10 min after the onset of injection (08:00–08:10). Events are colored by occurrence time with respect to the beginning of pumping and scaled by local magnitude. The treatment well (black line) and three perforation shots (solid red ellipsoids) of the nineteenth stage hydraulic fracturing treatment are also shown for reference. (b) Magnitude-frequency distribution of the detected events in (a), along with that of the conventional catalog (blue). The open diamonds mark the magnitude range over which the best fit slope, which corresponds to b value, was calculated. The bin spacing for both plots is 0.1 units. The b values of the two catalogues are 0.51 and 0.39, respectively.

there are a great number of relatively large events confined within a small volume to the northeast side of the injection interval. Figure 9b presents the magnitude-frequency distribution of the microseismicity from our approach, as well as that of the conventional catalog, with a b value of 0.51 ± 0.01 and 0.39 ± 0.01 , respectively. It is shown that our catalog lowers the magnitude of completeness by almost one unit of magnitude. Moreover, a more complete microseismic catalog within the lower magnitude range leads to a more robust estimate of b value. Consequently, the increased number of detected events by roughly an order of magnitude provides a higher level of detail in the spatiotemporal distribution of the microseismicity. In the companion paper, we investigate the detailed spatiotemporal evolution of the microseismicity and its possible relation to the fluid injection activity during the whole stage period.

To further compare the iMLT with the MFA, we processed the same continuous data set using the MFA with the same parameter setting. Besides the 10 master events within the first 10 min, there are only 238 additional microseismic events recovered with the MFA, compared to 326 events from our approach, implying that our approach can retrieve notably more events than the MFA. Figure 10a exhibits the coherence values of 238 events recovered by both approaches. The coherence values of the iMLT are apparently

generally increases with decreasing local magnitude (blue diamonds). The averaged lateral location error is approximately 52.5 m in the case of $M_L = -3.25$, which is probably due to the blurred coherence image resulting from the large error of the polarization direction estimation of low-SNR events. Therefore, we infer that the lateral location accuracy can be further improved with more favorable array geometry, for example, multiple-well monitoring array or hybrid surface downhole array. While the performance of polarization constraint is significantly degraded for extremely low SNR slave events, it can still provide reasonably low lateral location error (< 20 m) for low-magnitude events down to $M_L = 2.5$. In contrast, the vertical location errors are remarkably low over the magnitude range (purple diamonds), indicating that the focal depth can be well constrained, even for the extremely low SNR events. Overall, given the unfavorable array geometry and the high seismic noise, signals embedded in noise with magnitude down to -3.75 can still be robustly detected and located with reasonable accuracy based on the proposed approach. Of course, these results depend on the specific array geometry and the level of realistic ambient noise.

4. Field Data Set Example

We finally apply the proposed approach to a subset of continuous records during a single stage of hydraulic fracturing stimulation. With the clustering method described in section 2, we obtained 78 well located representative master events occurred during this treatment stage. The hypocentral distribution of the master events is shown in Figure 3 (open triangles), which generally shows a spatially uniform distribution.

Here we only analyze the results of the first 10 min continuous records (08:00–08:10). Besides 10 master events during this period, our approach recovers 326 additional microseismic events after removal of duplicate slave events, with an apparent magnitude of completeness (M_c) of -3.5 , compared to only 46 events in total in the conventional catalog. Figure 9a shows the map view of hypocentral distribution of the microseismic events. Events are color coded by occurrence time with respect to the onset of injection and scaled by local magnitude. The microseismic cloud extends several hundred meters along a NE-SW orientation, almost perpendicular to the wellbore. It is noted that

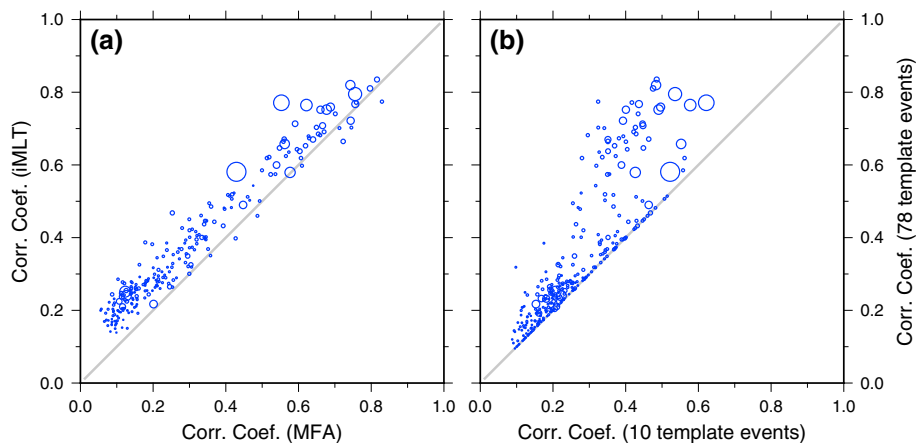


Figure 10. (a) Comparison of the coherence values of 238 slave events that are detected by both the matched filter analysis (MFA) and our approach. (b) Comparison of the coherence values of 294 slave events that are detected and located by the top 10 most prolific master events and all the 78 master events.

higher than that from the MFA, implying that these events are detected with higher confidence. Figure 11 exhibits the stacked cross correlograms at two individual grid nodes for one of the master events (20141110_082212). The first stacked cross correlogram corresponds to the grid node at the location of the master event, while the second one comes from the corrected stacking at the grid node (40, -80, and 20) relative to the hypocenter of the master event. It is apparent that there are notably more signals exceed the threshold in the cross correlogram from the iMLT stacking, suggesting that more slave events could be recovered.

Figure 12 presents the number of slave events detected by individual master event with iMLT (sky blue circles). The results from the MFA are also shown for comparison (gray circles). As expected, the number of slave events detected by each individual master event with iMLT is significantly larger than that of the MFA by virtue of allowing larger interevent separation. Moreover, the number of slave events by the MFA varies widely, which implies that the results could be notably affected by the choice of master events, if using only a few master events. The selection of a few nonprolific master events will greatly limit the detectability of the MFA. On the contrary, the iMLT approach does not suffer from this issue. The cumulative number of slave events is also obtained by retaining the master-slave event pairs with the highest coherence value (blue circles in Figure 12).

Surprisingly, the total number of slave events remains quasi-steady with more than 10 master events, which suggests that the later master events barely bring new slave events. Since microseismic events induced by hydraulic fracturing are commonly spatially clustered, a sparse set of representative master events may be capable of capturing waveform signature of all possible source types. Thus, they can detect most slave events, even the distance between master and slave events reaches a few wavelengths, especially considering the fact that our approach allows larger interevent separation. Caffagni et al. (2016) also argued that four uniformly distributed master events are sufficient for each treatment stage. Figure 10b presents the coherence values of 294 slave events that are detected by the top 10 most prolific master events and all the 78 ones, respectively. It is evident that the coherence values of the slave events from all the 78 master events are considerably higher than that from the top 10 master events, which is probably due to more proximal or more resembling to the extra master events. Therefore, while the additional master events might not drastically increase the number of slave events, they can potentially improve the location accuracy of the detected slave events.

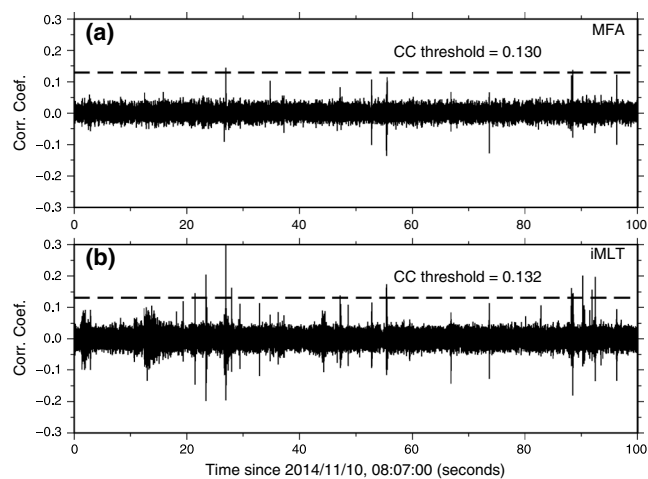


Figure 11. An example of stacked cross correlograms at two individual grid nodes, using master event 20141110_082212. (a) The grid node at the hypocenter of the master event; (b) the grid node (40, -80, and 20) relative to the hypocenter of the master event.

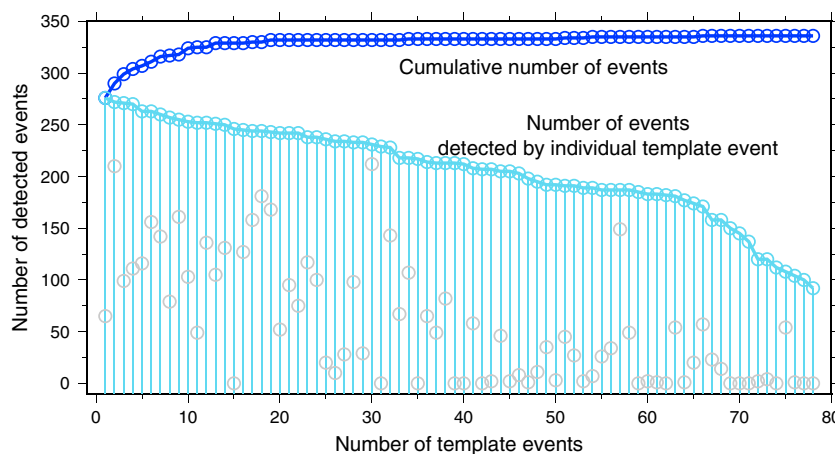


Figure 12. The number of slave events detected by individual master event using the matched filter analysis (gray circles) and our approach (sky blue circles). The cumulative number of slave events using our approach are denoted as blue circles. It is noted that duplicate slave events separated by less than 0.5 s are consolidated, by retaining the master-slave event pair with the highest coherence value.

5. Discussion

Similar to the MFA, the proposed iMLT requires a set of representative master events and is proved to be noise robust and exquisitely sensitive for detecting weak microseismic events that strongly resemble to proximal master events at low false alarm rates. This approach is different from previous coherence-based methods mainly in two ways.

First, at the slave event detection stage, the MFA assumes slave events are collocated with the corresponding master event, and consequently, the correlograms are stacked without moveout correction to account for the differential arrival times over the receiver array (e.g., Skoumal et al., 2015; Song et al., 2010). As illustrated in Figure 6a, in the case of large interevent separation, the stacking of misaligned waveforms (Figure 6c) results in low-amplitude and broadly spread pulses in the stacked cross correlogram and thus potentially leads to the failure in the matched filter detection, degrading the detectability of the MFA. Conversely, the iMLT searches for slave events using the moveout-corrected stacks of the correlograms in the detection stage. Generally, waveform similarity decreases with increasing interevent separation, depending on the heterogeneous structure near the source (Zhang & Wen, 2015). Typically, weak events are not visible on an individual waveform trace or cross correlogram. It is the coherent stacking that enable us to detect the tiny signals. Waveform coherence remarkably increases by making effective traveltime correction for the stacking process (Figure 6d). The stacking of cross correlograms along the corrected moveout, instead of assuming collocated master and slave events, results in stronger and more impulsive coherence signals (Figure 6b). The traveltime correction is the key factor in maximizing the coherence value, allowing detection of slave events with large separations from the master event (Figure 11) while keeping the false alarm rate at a reasonably low level. As a result, in the continuous data test, the iMLT detects 7 times more events (326 events) than the conventional catalog (46 events) and 37% more than the MFA detection (238 events) with the same parameter setting.

Second, we employed a different objective function in determining the location of a slave event relative to the master event with a grid search scheme. Caffagni et al. (2016) utilized the beamformed amplitude value of the waveform envelopes to search for the relative location of a slave event. On the contrary, we use the stacked cross correlogram as the objective function, which has several advantages over the envelope stacking. It suffers no coherence loss and thereby allows larger waveform variability, ensuring constructively stacking across large-aperture arrays. If the hypocentral distance between the master-slave event pair is significantly smaller than both the event receiver distance and the scale length of the velocity heterogeneity, the similar raypaths between the two events and a common receiver leads to nearly identical Green's functions. Consequently, the cross correlation eliminates the phases of the Green's function, leaving the relative phases of the source time functions of two closely located events (e.g., Hawthorne & Ampuero,

2017). Meanwhile, it also naturally accounts for any variations due to the radiation pattern of a typical double-couple source mechanism of shear sources. As a consequence, the cross correlograms should be identical, or quite similar if not, over the monitoring array so long as the spatial extent of the sources are small compared with the dominant seismic wavelength, regardless of the array configuration. Therefore, on one hand, all receivers contribute constructively to the cross correlograms stacking, which greatly enhances the ability to detect coherent signals immersed in strong ambient noise; on the other hand, this novel approach, tailored for linear downhole array configuration in this study, could be naturally extended to the case of multiple downhole array or large-aperture surface array or their combination without correction for radiation pattern, which can potentially improve lateral accuracy of extremely low SNR events. Furthermore, the slave events are located relatively to the corresponding master event. Hence, our location results are only slightly affected by the local velocity structure in the vicinity of the master events, without the need to take into account any intrinsic anisotropy and lateral heterogeneities in the velocity structure. Still, it should be kept in mind that the simplified 1-D velocity model used in this study may introduce location errors for the master events, thus slight shifts to the overall clusters.

This study successfully applies the M&L technique to microseismic monitoring in a reservoir scale, which is distinctly different from earthquake or nuclear test monitoring in regional or global scale (Zhang & Wen, 2014, 2015). The iMLT differs from the regular M&L technique in several key aspects. First, microseismic activity is typically monitored with linear downhole array, instead of widely distributed broadband stations. Accordingly, we introduce the P wave polarization constraint to resolve the horizontal extent of slave events in case of such unfavorable array geometry. Second, we calculate the cross correlograms of P and S waves separately, to reducing the effect of varying S - P traveltimes across the array, especially for the slave events with large interevent distance from the corresponding master event. Besides, it can also refrain from the cross correlograms being dominated by S wave owing to its relatively large amplitude. More importantly, the S - P traveltimes is essential for determining the hypocentral distance. Lastly, we propose an optimal procedure for selecting representative master events. Although the master events play a key role in enhancing the detectability of any template-based technique, the selection of optimal master events remains a contentious subject. As aforementioned, microseismic events induced by hydraulic fracturing are commonly spatially and temporally clustered. Nevertheless, repeated sources frequently produce varied waveforms not well represented by a single master event, possibly associated with the variable source mechanisms or source time functions, or contamination by transient noise signal occasionally. Additionally, the events may be scattered in a region larger than a few wavelengths at the dominant frequency. Thus, we first cluster all the events from a standard STA/LTA algorithm and then select the most prolific and uniformly distributed events from a given cluster, in order to form a complete basis for all potential microseismic events. It is worthy to point out that different configurations of clusters could be composed, depending on the correlation threshold for defining a doublet. However, we showed that our approach relaxes the restriction on the selection of master events to some extent, by virtue of allowing larger interevent separation and thus permitting greater waveform variability. On the contrary, the number of slaves events detected by individual master event could vary widely using the MFA (Figure 12). As a consequence, the results from the MFA appear to be strongly dependent on the selection of master events and thus might vary considerably from different combinations, which may lead to some slave events being omitted.

6. Conclusions

We have introduced an improved match and locate technique to robustly detect and accurately locate weak microseismic events based on waveform cross correlation. Our experiments using pseudo-synthetic events and real microseismic data set lead to the following conclusions: (1) By virtue of cross correlogram stacking of both P and S wave with moveout correction, this novel approach, which is tailored for downhole array geometry, further enhances the detectability of microseismic events associated hydraulic fracturing treatment, as compared with the matched filter analysis; (2) by locating the slave events relative to the corresponding master event, the proposed approach significantly improves the location precision, particularly the depth accuracy, even in the case of unfavorable array geometry; (3) the real microseismic data example demonstrates that a set of uniformly distributed master events yields an order of magnitude increase of locatable events compared with the conventional catalog, producing more easily interpretable spatiotemporal distribution of the microseismicity, which is addressed in detail in a companion paper.

Acknowledgments

We would like to thank Sichuan Geophysical Company of China National Petroleum Company (CNPC) for providing the field data set and permission to present this work. We are also grateful for the constructive comments and suggestions from two anonymous reviewers, which significantly improved the quality of this paper. This work was jointly supported by the National Basic Research Program of China (973 Program, 2015CB25093), the National Natural Science Foundation of China (41604043 and 41630209) and the Science Foundation of China University of Petroleum, Beijing (2462014YJRC045 and 2462015YQ1203). All the figures were made using the Generic Mapping Tools (GMT, Wessel et al., 2013). The example data are available from the corresponding author upon request.

References

- Akram, J., & Eaton, D. W. (2016). A review and appraisal of arrival time picking methods for downhole microseismic data. *Geophysics*, 81(2), KS71–KS91. <https://doi.org/10.1190/GEO2014-0500.1>
- Anikiev, D., Valenta, J., Stanek, F., & Eisner, L. (2014). Joint location and source mechanism inversion of microseismic events: Benchmarking on seismicity induced by hydraulic fracturing. *Geophysical Journal International*, 198(1), 249–258. <https://doi.org/10.1093/gji/ggu126>
- Arrowsmith, S. J., & Eisner, L. (2006). A technique for identifying microseismic multiplets and application to the Valhall field, North Sea. *Geophysics*, 71(2), V31–V40. <https://doi.org/10.1190/1.2187804>
- Bao, X., & Eaton, D. W. (2016). Fault activation by hydraulic fracturing in western Canada. *Science*, 354(6318), 1406–1409. <https://doi.org/10.1126/science.aag2583>
- Barrett, S. A., & Beroza, G. C. (2014). An empirical approach to subspace detection. *Seismological Research Letters*, 85(3), 594–600. <https://doi.org/10.1785/0220130152>
- Birnie, C., Chambers, K., Angus, D., & Stork, A. L. (2016). Analysis and models of pre-injection surface seismic array noise recorded at the Aquistore carbon storage site. *Geophysical Journal International*, 206(2), 1246–1260. <https://doi.org/10.1093/gji/ggw203>
- Caffagni, E., Eaton, D. W., Jones, J. P., & van der Baan, M. (2016). Detection and analysis of microseismic events using a matched filtering algorithm (MFA). *Geophysical Journal International*, 206(1), ggw168–ggw658. <https://doi.org/10.1093/gji/ggw168>
- Chen, H. C., Meng X., Niu F. L. and Tang Y. C. (2018). Microseismic monitoring of stimulating shale gas reservoir in SW China: 2. Spatial clustering controlled by the pre-existing faults and fractures. *Journal of Geophysical Research: Solid Earth*, 123. <https://doi.org/10.1002/2017JB014491>
- Drew, J., White, R. S., Tilmann, F., & Tarasewicz, J. (2013). Coalescence microseismic mapping. *Geophysical Journal International*, 195(3), 1773–1785. <https://doi.org/10.1093/gji/ggt331>
- Duncan, P. M., & Eisner, L. (2010). Reservoir characterization using surface microseismic monitoring. *Geophysics*, 75(5), 75A139–75A146. <https://doi.org/10.1190/1.3467760>
- Eaton, D. W., & Caffagni, E. (2015). Enhanced downhole microseismic processing using matched filtering analysis (MFA). *First Break*, 33, 49–55.
- Gharti, H. N., Oye, V., Roth, M., & Kuhn, D. (2010). Automated microearthquake location using envelope stacking and robust global optimization. *Geophysics*, 75(4), MA27–MA46. <https://doi.org/10.1190/1.3432784>
- Gibbons, S. J., & Ringdal, F. (2006). The detection of low magnitude seismic events using array-based waveform correlation. *Geophysical Journal International*, 165(1), 149–166. <https://doi.org/10.1111/j.1365-246X.2006.02865.x>
- Grigoli, F., Cesca, S., Amoroso, O., Emolo, A., Zollo, A., & Dahm, T. (2013). Automated seismic event location by waveform coherence analysis. *Geophysical Journal International*, 196(3), 1742–1753. <https://doi.org/10.1093/gji/ggt477>
- Grigoli, F., Cesca, S., Krieger, L., Kriegerowski, M., Gammaldi, S., Horalek, J., et al. (2016). Automated microseismic event location using master-event waveform stacking. *Scientific Reports*, 6(1). <https://doi.org/10.1038/srep25744>
- Hawthorne, J. C., & Ampuero, J. P. (2017). A phase coherence approach to identifying co-located earthquakes and tremor. *Geophysical Journal International*, 209, 623–642. <https://doi.org/10.1093/gji/ggx012>
- Hutton, L. K., & Boore, D. M. (1987). The M_L scale in southern California. *Bulletin of the Seismological Society of America*, 25, 1–32.
- Kao, H., & Shan, S. (2004). The source-scanning algorithm: Mapping the distribution of seismic sources in time and space. *Geophysical Journal International*, 157(2), 589–594. <https://doi.org/10.1111/j.1365-246X.2004.02276.x>
- Liao, Y. C., Kao, H., Rosenberger, A., Hsu, S. K., & Huang, B. S. (2012). Delineating complex spatiotemporal distribution of earthquake aftershocks: An improved source-scanning algorithm. *Geophysical Journal International*, 189(3), 1753–1770. <https://doi.org/10.1111/j.1365-246X.2012.05457.x>
- Maxwell, S. C., Rutledge, J., Jones, R., & Fehler, M. (2010). Petroleum reservoir characterization using downhole microseismic monitoring. *Geophysics*, 75(5), 75A129–75A137. <https://doi.org/10.1190/1.3477966>
- Peng, Z., & Zhao, P. (2009). Migration of early aftershocks following the 2004 Parkfield earthquake. *Nature Geoscience*, 2(12), 877–881. <https://doi.org/10.1038/NGEO697>
- Pesicek, J. D., Child, D., Artman, B., & Cieslik, K. (2014). Picking versus stacking in a modern microearthquake location: Comparison of results from a surface passive seismic monitoring array in Oklahoma. *Geophysics*, 79(6), KS61–KS68. <https://doi.org/10.1190/GEO2013-0404.1>
- Rutledge, J. T., & Phillips, W. S. (2003). Hydraulic stimulation of natural fractures as revealed by induced microearthquakes, Carthage Cotton Valley gas field, east Texas. *Geophysics*, 68(2), 441–452. <https://doi.org/10.1190/1.1567214>
- Shelly, D. R. (2010). Migrating tremors illuminate complex deformation beneath the seismogenic San Andreas fault. *Nature*, 463(7281), 648–652. <https://doi.org/10.1038/nature08755>
- Shelly, D. R., Beroza, G. C., & Ide, S. (2007). Non-volcanic tremor and low-frequency earthquake swarms. *Nature*, 446(7133), 305–307. <https://doi.org/10.1038/nature05666>
- Skoumal, R. J., Brudzinski, M. R., & Currie, B. S. (2015). Distinguishing induced seismicity from natural seismicity in Ohio: Demonstrating the utility of waveform template matching. *Journal of Geophysical Research: Solid Earth*, 120, 6284–6296. <https://doi.org/10.1002/2015JB012265>
- Song, F., Warpinski, N. R., Toksoz, M. N., & Kuleli, H. S. (2014). Full-waveform based microseismic event detection and signal enhancement: An application of the subspace approach. *Geophysical Prospecting*, 62(6), 1406–1431. <https://doi.org/10.1111/1365-2478.12126>
- Song, F. X., Keluli, H. S., Toksoz, M. N., Ay, E., & Zhang, H. J. (2010). An improved method for hydrofracture-induced microseismic event detection and phase picking. *Geophysics*, 75(6), A47–A52. <https://doi.org/10.1190/1.3484716>
- Stanek, F., Anikiev, D., Valenta, J., & Eisner, L. (2015). Semblance for microseismic event detection. *Geophysical Journal International*, 201(3), 1362–1369. <https://doi.org/10.1093/gji/ggv070>
- Trojanowski, J., & Eisner, L. (2016). Comparison of migration-based location and detection methods for microseismic events. *Geophysical Prospecting*, 65(1), 47–63. <https://doi.org/10.1111/1365-2478.12366>
- Vaezi, Y., & van der Baan, M. (2014). Analysis of instrument self-noise and microseismic event detection using power spectral density estimates. *Geophysical Journal International*, 197(2), 1076–1089. <https://doi.org/10.1093/gji/ggu036>
- van der Elst, N., Savage, H. M., Karanen, K. M., & Abbers, G. A. (2013). Enhanced remote earthquake triggering at fluid-injection sites in the Midwestern United States. *Science*, 341(6142), 164–167. <https://doi.org/10.1126/science.1238948>
- Waldhauser, F., & Ellsworth, W. L. (2000). A double-difference earthquake location algorithm: Method and application to the northern Hayward fault, California. *Bulletin of the Seismological Society of America*, 90(6), 1353–1368. <https://doi.org/10.1785/0120000006>
- Warpinski, N. (2009). Microseismic monitoring: Inside and out. *Journal of Petroleum Technology*, 61(11), 80–85. <https://doi.org/10.2118/118537-JPT>
- Wessel, P., Smith, W. H. F., Scharroo, R., Luis, J. F., & Wobbe, F. (2013). Generic mapping tools: Improved version released. *Eos, Transactions American Geophysical Union*, 94(45), 409–410. <https://doi.org/10.1002/2013EO450001>

- Williams-Stroud, S., Ozgen, C., & Billingsley, R. L. (2013). Microseismicity-constrained discrete fracture network models for stimulated reservoir simulation. *Geophysics*, 78(1), B37–B47. <https://doi.org/10.1190/geo2011-0061.1>
- Zhang, M., & Wen, L. X. (2014). Seismological evidence for a low-yield nuclear test on 12 May 2010 in North Korea. *Seismological Research Letters*, 86(1), 138–145. <https://doi.org/10.1785/02201401170>
- Zhang, M., & Wen, L. X. (2015). An effective method for small event detection: Match and locate (M&L). *Geophysical Journal International*, 200(3), 1523–1537. <https://doi.org/10.1093/gji/ggu466>